



# Phase field modeling of fracture in rubbery polymers. Part I: Finite elasticity coupled with brittle failure



Christian Miehe\*, Lisa-Marie Schänzel

Institute of Applied Mechanics (CE), Chair I, University of Stuttgart, Pfaffenwaldring 7, 70550 Stuttgart, Germany

## ARTICLE INFO

### Article history:

Received 23 November 2012

Received in revised form

6 May 2013

Accepted 20 June 2013

Available online 31 July 2013

### Keywords:

Rubbery polymers

Fracture

Phase field modeling

Finite strain

Coupled multi-field problem

## ABSTRACT

This work presents a new phase field model for rate-independent crack propagation in rubbery polymers at large strains and considers details of its numerical implementation. The approach accounts for micro-mechanically based features of both the elastic bulk response as well as the crack toughness of idealized polymer networks. The proposed *diffusive* crack modeling based on the introduction of a crack phase field overcomes difficulties associated with the computational realization of *sharp* crack discontinuities, in particular when it comes to complex crack topologies. The crack phase field governs a crack density function, which describes the macroscopic crack surface in the polymer per unit of the reference volume. It provides the basis for the constitutive modeling of a degrading free energy storage and a crack threshold function with a Griffith-type critical energy release rate, that governs the crack propagation in the polymer. Both the energy storage as well as the critical energy release due to fracture can be related to classical statistical network theories of polymers. The proposed framework of diffusive fracture in polymers is formulated in terms of a rate-type variational principle that determines the evolution of the coupled primary variable fields, i.e. the deformation field and the crack phase field. On the computational side, we outline a staggered solution procedure based on a one-pass operator split of the coupled equations, that successively updates in a typical time step the crack phase field and the displacement field. Such a solution algorithm is extremely robust, easy to implement and ideally suited for engineering problems. We finally demonstrate the performance of the phase field formulation of fracture at large strains by means of representative numerical examples.

© 2013 Elsevier Ltd. All rights reserved.

## 1. Introduction

The prediction of failure mechanisms due to crack initiation and propagation in rubber-like materials is of great importance for engineering applications. Practical applications are the modeling of fracture phenomena in tires, seals, medical devices, conveyor belts and base isolations of buildings. A rubbery polymer may exhibit a very complicated inelastic behavior at finite strains. Besides its complex highly non-linear elasticity, complicated inelastic features such as visco-elastic-plastic phenomena and the so-called Mullins' effect of strain-softening occur, see for example Miehe and Keck (2000) and references cited therein for a purely macroscopic account. In this first part of our work on fracture in rubbery polymers, we focus on crack propagation in rubbers with an *idealized purely elastic response*. This is typically achieved for very *slow deformation processes*, where viscous effects can be neglected. For this scenario, we outline a new phase field approach to crack propagation, which embeds micro-mechanically based network theories of both the elastic bulk response as well as the crack toughness.

\* Corresponding author. Tel.: +49 711 685 66379; fax: +49 711 685 66347.

E-mail addresses: [christian.miehe@mechbau.uni-stuttgart.de](mailto:christian.miehe@mechbau.uni-stuttgart.de), [cm@mechbau.uni-stuttgart.de](mailto:cm@mechbau.uni-stuttgart.de) (C. Miehe).

URL: <http://www.mechbau.uni-stuttgart.de/> (C. Miehe).

### 1.1. Elastic bulk response of rubbery polymers at finite strains

The *elastic bulk response* of rubbery polymers is dominated by an extreme reformability and can be well explained by statistical micro-mechanics, see for example Treloar (1975) for an introduction. Rubber elasticity is achieved by a molecular micro-structure consisting of very flexible and mobile long chain molecules and a three-dimensional network that is formed by occasional cross-links between molecules. The dominant contribution to the elastic response of rubber-like materials is due to changes in conformations of network constituents, yielding the so-called entropy elasticity theory. Entropic elasticity of chain molecules is well established in the context of statistical mechanics, see Kuhn (1934, 1936), Kuhn and Gr $\ddot{u}$  n (1942), Treloar (1975), Flory (1989) and references cited therein. In the literature, many constitutive models for the macroscopic elastic response of rubbery polymers have been developed, see Boyce and Arruda (2000) and Miehe et al. (2004) for an overview. *Purely phenomenological macro-models* involve invariant or principal stretch based isotropic free energy functions, often having polynomial structures. The most advanced formulations are those of Ogden (1972, 1984). However, these approaches lack relations to the molecular structure of the material. This is achieved by *micro-mechanically based network models*, such as the three chain model proposed by James and Guth (1943), the eight chain model suggested by Arruda and Boyce (1993) and the affine full network models considered in Treloar (1946), Treloar and Riding (1979) and Wu and van der Giessen (1993). It is well-known that the affinity assumption between microscopic and macroscopic deformation is not in agreement with experimental observations, in particular in the range of large deformations. Consequently, Boyce and Arruda (2000) argued that the eight chain model yields more realistic results than the seemingly more precise affine full network models. A further improvement provides the non-affine micro-sphere model proposed in Miehe et al. (2004), which allow a flexible modeling of the locking stretches in multi-dimensional deformations. The above mentioned micro-mechanically based models consider idealized polymer networks with free motions of its single chains. However, in real networks topological constraint effects arise due to entanglement-like formations. Molecular-based statistical approaches that incorporate these effects are *constrained junction theories* which formulate the topological constraints around the junctions and the *constrained segment theories*. The constraint junction part of the model proposed by Flory and Erman (1982) was used by Boyce and Arruda (2000) to improve the performance of the eight chain model. The constraint segment approach is consistent with the so-called tube models of rubber elasticity, see for example Deam and Edwards (1976), Edwards and Vilgis (1988), Heinrich and Straube (1983) and Heinrich and Kaliske (1997). In Miehe et al. (2004), we equipped the micro-sphere model with a characteristic micro-tube deformation that is linked to the macroscopic deformation. This microsphere model with a low number of physically based material parameters shows an excellent fit to experimental results. The phase field model of fracture in polymers developed in this work allows the *incorporation of all the above mentioned models* for the bulk response rubbers.

### 1.2. Fracture toughness of rubbery polymers at finite strains

Similar to the elastic bulk response, the *fracture toughness* of rubbery polymers can be rooted in statistical micro-mechanics. The occurrence of macroscopic fracture of rubbery polymers is a result of the failure of the network at the molecular level. When a rubber-like material is deformed, the network constituents change their conformation and polymer chains align according to the above mentioned bulk models. At a critical load level, rupture of one first molecule occurs, inducing the overload and breakage of neighboring chains. Further loading of the body involves rupture of additional chains and finally a macroscopic crack is generated. Early investigations of failure of rubbers were performed in a sequence of papers by Rivlin and Thomas (1953), Thomas (1955), Greensmith and Thomas (1955) and Greensmith (1956). Here, a *critical macroscopic fracture toughness or tearing energy for rubbers* was defined in the sense of a critical energy release rate in line with the classical approach to fracture by Griffith (1920). In a pioneering work, Lake and Thomas (1967), explained these experimental observations by a simple *molecular-theoretical model*, which determines this critical surface energy in terms of the parameters of the network. It turned out that the energy to create a new crack surface predicted by this micro-mechanical model is much less than the tearing energy measured in the above mentioned works. The difference can be explained by *additional dissipative mechanisms* in the material that surrounds the crack tip, see for example Persson et al. (2005) for a recent review. Energy dissipation at the advancing crack in a viscoelastic solid has two contributions. The first is associated with the *innermost region at the crack tip*, where a new macroscopic crack surface is created by chain pull out and bond breaking. This contribution is related to the basic molecular strength of the material and the theoretical prediction of Lake and Thomas (1967). The second contribution comes from the viscoelastic dissipation in front of the crack tip, see for example Persson and Brener (2005) and Kroon (2011). This implies that the critical tearing energy of rubber depends strongly on both the temperature as well as the crack tip velocity. However, as noted by Ahagon and Gent (1975), a reasonable good agreement with the theoretical results of Lake and Thomas (1967) can be obtained in experimental measurements under near equilibrium conditions, such as reported in Mueller and Knauss (1971). They succeeded in measuring low tearing energies, independent of the rate of crack propagation and temperature, by employing low rates of tear. In this first part of the work, we focus on such a scenario and *neglect viscoelastic effects*.

### 1.3. A phase field modeling approach to brittle fracture

The recent works Miehe et al. (2010a, 2010b) outline a general thermodynamically consistent framework for the *phase field modeling of crack propagation at small-strains*. The formulation is essentially a gradient damage theory, however, with critical ingredients rooted in fracture mechanics. This concerns in particular the introduction of a *crack surface density function*  $\gamma_1(d, \nabla d)$ ,

depending on a length scale  $l$ , which measures a spatially regularized total crack surface

$$\Gamma_l(d) = \int_B \gamma_l(d, \nabla d) dV \quad (1)$$

with respect to the volume of the solid's reference configuration  $B$ . It is a function of the crack phase field  $d \in [0, 1]$ , which interpolates between the unbroken and the broken state of the material in the sense of a scalar damage variable. The function  $\gamma_l$  can be motivated by a prescribed shape of the regularization of sharp cracks, as considered in Miehe et al. (2010b), but also appeared before in  $\Gamma$ -convergence regularizations of free discontinuity problems as proposed in Ambrosio and Tortorelli (1990, 1992), Dal Maso (1993) and Braides (2002, 1998). The crack surface density function  $\gamma_l$  provides the starting point for a continuum damage formulation of fracture. In particular, *surface integrals* defined on sharp crack surfaces  $\Gamma \subset B$  are *approximated by volume integrals*, such as the critical fracture energy

$$\int_\Gamma g_c dA \approx \int_B g_c \gamma_l dV, \quad (2)$$

where  $g_c$  is the Griffith-type critical energy release rate. Hence,  $g_c \gamma_l$  can be viewed as a critical *fracture energy* measured with respect to the unit volume of the solid's reference configuration. Assuming an elastic free energy storage function  $\psi(\nabla \phi; d)$  in the bulk of the solid depending on the deformation gradient  $\nabla \phi$ , that degrades for increasing phase field  $d$ , the *evolution of the phase field* was proposed in Miehe et al. (2010b)

$$\dot{d} = \frac{1}{\eta} \left\langle -\frac{\delta(\psi + g_c \gamma_l)}{\delta d} \right\rangle \quad (3)$$

as a non-smooth, *local* equation. This equation *modifies* classical Ginzburg–Landau– or Allen–Cahn-type evolution equations too a phase field model of fracture, where the phase field is interpreted as a local, monotonously growing damage variable. It makes the evolving phase field dependent on the variational derivative of a total energy density, consisting of the elastic bulk energy  $\psi$  and the regularized surface energy  $g_c \gamma_l$ . The parameter  $\eta$  plays the role of a viscosity for the crack evolution and provides for  $\eta \rightarrow 0$  the *rate-independent limit*. The non-smooth structure, governed by the McAuly bracket  $\langle \cdot \rangle$ , as well as the interpretation of the parameter  $\eta$  as a viscous regularization that may vanish, marks a key difference to the smooth phase field models of fracture proposed by Hakim and Karma (2009) and Karma et al. (2001), which are based on the classical Ginzburg–Landau equation. It is also different from the variational theory of brittle fracture proposed by Francfort and Marigo (1998), Bourdin et al. (2008), that uses the above mentioned concepts of  $\Gamma$ -convergence by introducing a scalar auxiliary field in a *global* variational context, without arriving at a local evolution equation of the type (3).

Note that the above Eqs. (1)–(3) contain the basic ingredients of brittle fracture mechanics, however, in a regularized continuum sense of *gradient damage mechanics*. The formulation can be embedded into the general theory of gradient-extended dissipative continua with length scales, such as outlined in a general context in Capriz (1989), Mariano (2001), Frémond (2002) and the recent work Miehe (2011) on its variational structure. In particular, our approach to phase field fracture is conceptually in line with theories of gradient damage outlined in Frémond and Nedjar (1996) and Peerlings et al. (1996), however, with *critical differences* in the choice of the free energy and dissipation potential functions. Recall that finite-element-based numerical implementations of *sharp crack discontinuities*, such as interface element formulations (Xu and Needleman, 1993; Ortiz and Pandolfi, 1999; Miehe and Gürses, 2007; Gürses and Miehe, 2009), element enrichment strategies (Simo et al., 1993; Oliver, 1996a, 1996b; Linder and Armero, 2009) and nodal enrichment strategies (Moës et al., 1999; Wells and Sluys, 2001; Gasser and Holzapfel, 2005; Belytschko et al., 2003; Song and Belytschko, 2009), suffer in three-dimensional applications with complex crack branching. In contrast, phase-field-type diffusive crack approaches are *smooth* continuum formulations which avoid the modeling of discontinuities and can be implemented in a straightforward manner by coupled multi-field finite element solvers. Complex crack patterns can be modeled without any changes in algorithmic structure for sufficiently fine mesh resolutions.

In this work we advance our above mentioned approach to the analysis of fracture in polymer materials undergoing finite strains. The goal is to design a continuum theory of crack propagation for rubber-like materials for the rate-independent limit, which accounts for the above mentioned micro-mechanical roots of the bulk response and the fracture toughness. We start our investigation in Section 2 with a short review of the micro-mechanical basis. This concerns the outline of models for the *elastic bulk stiffness* and the *fracture toughness* of polymer networks obtained for statistical mechanics, which serve as the basis for the subsequent treatment. A descriptive motivation of a regularized crack topology based on a phase field is given in Section 3. This treatment results in the definition of a *crack surface functional*, depending on the crack phase field, that  $\Gamma$ -converges for vanishing length-scale parameter to a sharp crack topology. The crack phase field is introduced as a Lagrangian object defined on the reference configuration. The crack opening is visualized on the deformed configuration as a *level set of the phase field*.

Section 4 outlines a *variational principle* for the continuous evolution problem of the governing deformation and phase fields. To this end, we introduce functionals for the evolution of the stored energy, the dissipation and the power due to external loads. The energy is governed by the micro-mechanical network model for the bulk response and a specific crack degradation function, and regularized by the gradient term of the crack surface functional. A dual dissipation potential function is obtained from the concept of maximum dissipation, based on a threshold function related to the local part of the crack surface functional. The growth of the threshold is governed by the micro-mechanically based critical energy release. We then derive all governing equations of the coupled problem as the Euler equations of a saddle point principle that optimizes a rate potential. A compact formulation of the governing equations is obtained by the introduction of a local history field. It contains the maximum reference

stored bulk energy in the deformation history, which may be considered as a measure for the maximum strain in history. For this coupled field problem, we develop in Section 5 a staggered solution scheme. The operator splitting essentially constitutes a phase field predictor followed by an elastic corrector. The algorithm is extremely robust and considered to be the canonically simple scheme for the treatment of diffusive fracture in elastic solids. Finally, Section 6 outlines representative numerical examples which demonstrate the capability of the proposed phase field models of fracture in rubbery polymers.

## 2. Micromechanical modeling of bulk elasticity and failure

An important aspect of this paper is to outline an approach to fracture in rubbery polymers that is micromechanically motivated, and takes into account the network structure of crosslinked polymer chains. We show in this section that the basic two macroscopic parameters used in the subsequent part of the paper, the *elastic bulk stiffness*  $\mu$  as well as the *fracture toughness*  $g_c$ , are linked by concepts of statistical mechanics to the microstructure of the polymer network.

### 2.1. Micromechanically motivated stiffness of a polymer network

In classical entropic elasticity of polymer networks, the entropy  $s$  of a single polymer chain is governed by the Boltzmann equation. Hence, the free energy of a chain is

$$\psi = -\theta s \quad \text{with} \quad s = k \ln p, \quad (4)$$

where  $p$  is the probability density that describes the free chain response.  $k$  is the Boltzmann constant and  $\theta > 0$  the absolute temperature. Now consider a single polymer consisting of  $N$  segments of equal length  $l$  as depicted in Fig. 1a. The classical Gaussian statistics derived by Kuhn (1934, 1936) considers the unconstrained chain with end-to-end distance  $r := |\mathbf{r}| \ll L := Nl$  much smaller than the contour length  $L$ , i.e. moderate deformations of the chain. Here, the probability density per unit volume of a randomly jointed chain characterized by the end-to-end vector  $\mathbf{r}$  has the form

$$p(\mathbf{r}) = p_0 \exp\left[-\frac{3}{2}\lambda^2\right] \quad \text{with} \quad p_0 := (3/2Nl^2\pi)^{3/2}, \quad (5)$$

see Treloar (1975) p. 47, in terms of the stretch  $\lambda := r/r_0 \in [0, \sqrt{N}]$ . Here,  $r_0 := \sqrt{N}l$  is the random-walk mean-square distance of a chain. Insertion of (5) into (4) gives the *free energy of the chain*

$$\psi(\lambda) = \frac{3}{2}k\theta\lambda^2 \quad (6)$$

as a function of the stretch  $\lambda$ . The simplest *network model* that links the response of a single polymer chain to the macroscopic deformation of a continuum is the *three-chain model*, which can be traced back to Kuhn and Gr $\ddot{u}$  n (1942) and James and Guth (1943). It considers a network of  $n$  chains per unit volume and links the microscopic stretch  $\lambda$  of a single strain embedded in the continuum by an *affine deformation assumption* to the three macroscopic principal stretches

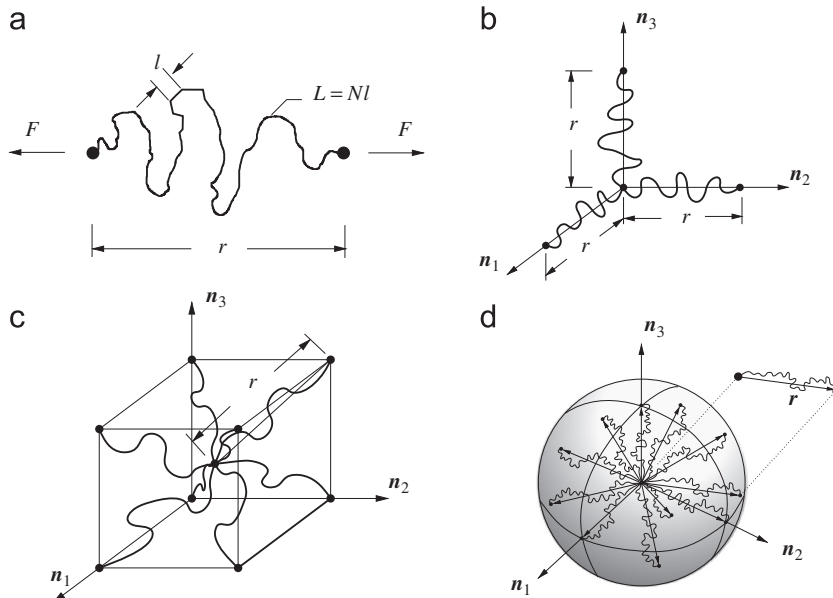


**Fig. 1.** Network models for rubbery polymers. (a) Single chain with  $N$  segments of length  $l$ , end-to-end distance  $r$  and contour length  $L = Nl$ , (b) three chain model: chains in principal stretch directions  $\mathbf{n}_i$ , (c) eight-chain model: chains placed along the space-diagonals of a cube, all undergoing the same stretch and (d) micro-sphere model: chain orientation continuum with directors  $\mathbf{r}$ , stretch fluctuation determined by a principle of minimum averaged energy.

$\{\lambda_i\}_{i=1,3}$  of the continuum, obtained by the singular value decomposition of the (isochoric) deformation gradient

$$\mathbf{F} := \nabla \boldsymbol{\varphi}(\mathbf{X}) = \sum_{i=1}^3 \lambda_i \mathbf{n}_i \otimes \mathbf{N}_i \quad \text{with} \quad \det[\mathbf{F}] = 1 \quad (7)$$

at a typical point  $\mathbf{X} \in \mathcal{B}$  of the continuum  $\mathcal{B} \subset \mathcal{R}^3$ . The macroscopic free energy of the continuum is constructed by taking the arithmetic average of *three representative chain energies* aligned with the macroscopic principal stretch directions as depicted in Fig. 1b, i.e.

$$\Psi = n \langle \psi \rangle \quad \text{with} \quad \langle \psi \rangle := \frac{1}{3} [\psi(\lambda_1) + \psi(\lambda_2) + \psi(\lambda_3)]. \quad (8)$$

Insertion of into (6) into (8) and taking into account  $\text{tr}[\mathbf{F}^T \mathbf{F}] = \lambda_1^2 + \lambda_2^2 + \lambda_3^2$  finally gives the classical closed-form *macroscopic free energy function* of the polymer network

$$\Psi(\mathbf{F}) = \frac{\mu}{2} \text{tr}[\mathbf{F}^T \mathbf{F}] \quad \text{with} \quad \mu = nk\theta. \quad (9)$$

The macroscopic elastic response of the rubber-like material is the governed by a *principle of minimum potential energy*

$$\boldsymbol{\varphi} = \text{Arg} \left\{ \inf_{\boldsymbol{\varphi}} \int_{\mathcal{B}} \Psi(\nabla \boldsymbol{\varphi}) dV \right\}, \quad (10)$$

that determines the deformation map  $\boldsymbol{\varphi} : \mathbf{X} \mapsto \mathbf{x}$  of the continuum. In continuum mechanics, this energy function is known as the Neo-Hookean free energy, which has through the above treatment a well-defined micromechanically motivated *network stiffness*  $\mu$ . More advanced network theories of rubbery polymers applicable to large deformations replace the Gaussian statistics by the *inverse Langevin statistics*, developed by Kuhn and Gr $\ddot{u}$  n (1942) and James and Guth (1943), which takes account for the finite extensibility of the chain. It results in the free energy of a single chain

$$\psi(\lambda) = Nk\theta \left( \lambda_r \mathcal{L}^{-1}(\lambda_r) + \ln \frac{\mathcal{L}^{-1}(\lambda_r)}{\sinh \mathcal{L}^{-1}(\lambda_r)} \right), \quad (11)$$

which advances (6) for end-to-end distances  $r$  up to the limiting value  $L$ . Here,  $\mathcal{L}(x) = \coth x - 1/x$  is the well-known Langevin function, see Treloar (1975) p. 103, and  $\lambda_r := r/L = \lambda/\sqrt{N} \in [0, 1)$  the relative stretch. Furthermore, the restrictive affine deformation assumption can be relaxed by more advanced network models, such as the *non-affine micro-sphere network model* developed in Miehe et al. (2004), that links by a particular homogenization method on the unit sphere  $S \subset \mathcal{R}^2$  depicted in Fig. 1d the micro-stretch  $\lambda$  of the single chain to the macroscopic deformation gradient (7) by the p-root average of the macroscopic stretch

$$\langle \bar{\lambda} \rangle_p := \left[ |S|^{-1} \int_S \bar{\lambda}^p dA \right]^{1/p} \quad \text{with} \quad \bar{\lambda} := |\mathbf{F} \mathbf{r}|, \quad (12)$$

where  $\mathbf{r}$  is the unit director to the surface of the sphere. The macroscopic free energy of the non-affine network model is derived as

$$\Psi(\mathbf{F}) = n\psi(\langle \bar{\lambda} \rangle_p). \quad (13)$$

This function describes the idealized network with free fluctuation of the chains between the cross-links of the network. An additional free energy representing the energy due to interaction of chain is added. The model is based on five physically motivated material parameters and shows excellent fits to multi-dimensional experimental results, as demonstrated in Fig. 2. We refer to Miehe et al. (2004) for more details.  $p > 0$  in (12) is a material parameter. For  $p=2$ , the micro-sphere

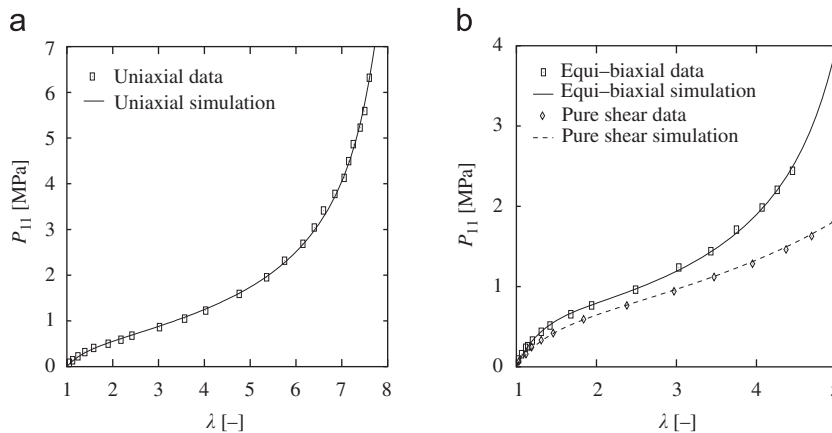


**Fig. 2.** Performance of the non-affine micro-sphere model developed in Miehe et al. (2004). Fit of multi-dimensional test data from Treloar (1944) with five micromechanically motivated material parameters  $\mu = 0.292$  MPa,  $N = 22.01$ ,  $p = 1.472$ ,  $U = 0.744$ ,  $q = 0.1086$ . (a) uniaxial deformation and (b) equi-biaxial and pure shear deformation.



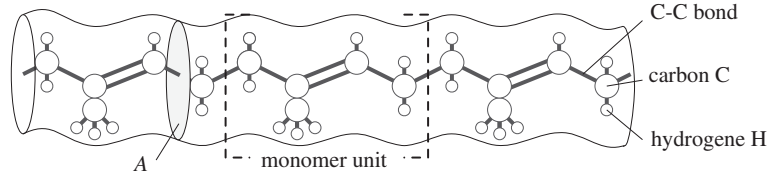


**Fig. 3.** Molecular structure of natural rubber. The polymer molecule consists of  $N$  monomer units (isoprene) with cross-sectional area  $A$ . The breaking of a C–C bond gives a first estimate of the energy release rate and the fracture toughness.

model degenerates to the *eight chain model* proposed by [Arruda and Boyce \(1993\)](#) and visualized in [Fig. 1c](#),

$$\Psi(\mathbf{F}) = n\psi(\langle \bar{\lambda} \rangle_2) \quad \text{with} \quad \langle \bar{\lambda} \rangle_2 = \sqrt{\text{tr}[\mathbf{F}^T \mathbf{F}]/3}, \quad (14)$$

which is simpler due to its closed-form relationship to the invariant  $\text{tr}[\mathbf{F}^T \mathbf{F}]$  of  $\mathbf{F}$  but of limited fitting capability. This summarizes our overview about physically motivated network models of rubber-like polymers. Further details can be found in the textbooks [Treloar \(1975\)](#), [Flory \(1989\)](#) and [Doi and Edwards \(1986\)](#), as well as in the papers [Boyce and Arruda \(2000\)](#) and [Miehe et al. \(2004\)](#).

## 2.2. Micromechanically motivated fracture toughness of a network

Basic ingredients of fracture in rubbers at finite strains can also be micro-mechanically motivated by a network theory. [Rivlin and Thomas \(1953\)](#) examined how energetic considerations of the stored energy can be used to describe a criterion for tearing in rubbery polymers. Their considerations based on the classical criterion of brittle fracture suggested by [Griffith \(1920\)](#) predicts crack propagation if the *energy release rate*, i.e. the change in elastic strain energy per unit area of crack growth

$$g := -\frac{\delta}{\delta \Gamma} E_r(\varphi) \quad \text{with} \quad E_r(\varphi) = \inf_{\varphi} \int_{B_r} \Psi(\nabla \varphi) dV, \quad (15)$$

reaches a *critical value*  $g_c$ . Here,  $\Gamma$  is the crack surface generated inside of the body  $B_r$  and  $\delta(\cdot)/\delta \Gamma$  the variational or functional derivative of the stored bulk energy  $E_r$ .  $\Psi$  is the stored energy function obtained by the micromechanical network models outlined above, see (9), (13) or (14). [Rivlin and Thomas \(1953\)](#) recorded for several test specimens the load–displacement relations up to a point of rupture at a constant overall deformation of the test piece. The work done until rupture was evaluated and related to the initial cut length to get a relation between increase in cut length and work done. From the slope of these curves they identified test values of the critical energy release rate  $g_c$ .

In a pioneering work, [Lake and Thomas \(1967\)](#), explained these experimental observations by a simple micromechanical model, which determines the critical energy release rate  $g_c$ . They considered the rupture of rubber by analyzing the rupture of a polymer molecule as schematically depicted in [Fig. 3](#). A first estimate of fracture toughness is achieved by the analysis of the break up of chemical bonds between the carbon atoms in the polymer chain. The monomer unit (isoprene) of the natural rubber depicted in [Fig. 3](#) has a cross-sectional area  $A$  and the average dissociation energy  $U$  of the C–C bonds. Thus the surface energy for rupture of a monomer is

$$g_{\text{monomer}} = U/A. \quad (16)$$

This simple analysis of monomer rupture dramatically underestimates experimental results of rubbers, because it does not take into account the real microstructure consisting of flexible long-chain molecules that form a network via crosslinks. As a consequence, [Lake and Thomas \(1967\)](#) analyzed a chain as depicted in [Fig. 4](#), i.e. the part of a molecule lying in between two crosslinks, which lie on opposite sides of the plane where the crack is expected to propagate. Similar to [Fig. 1a](#), the chain consists of  $N$  monomer units with end-to-end distance between the two crosslinks  $r := |\mathbf{r}|$ . To break a particular bond within the chain, it is necessary to subject all other bonds, which are lying in the same chain, by the same breaking force. Each unit in the chain must be strained up to rupture before the chain will break. If the surface energy required to rupture a monomer unit is  $g_{\text{monomer}}$  defined in (16), the *energy required to rupture a single chain* consisting of  $N$  monomers is

$$g_{\text{chain}} = N g_{\text{monomer}}. \quad (17)$$

In order to get the *energy required to rupture a network*, we apply the Gaussian statistics for the probability density  $p(\mathbf{r})$  per unit volume of a randomly jointed chain already defined in (5). Then, the probability density per unit of the radius  $r$  of a sphere is obtained by multiplying  $p(\mathbf{r})$  with the surface area  $S := 4\pi r^2$

$$P(r) = p(\mathbf{r})S = 4\pi r^2 p_0 \exp\left[-\frac{3}{2}\lambda^2\right], \quad (18)$$

see [Treloar \(1975\)](#) p. 50. Then, the *mean end-to-end distance* of the chains is

$$\bar{r} = \int_0^\infty r \cdot P(r) dL = \int_0^\infty 4\pi r^3 p_0 \exp\left[-\frac{3}{2}r^2/Nl^2\right] dr = \sqrt{\frac{8N}{3\pi}} l. \quad (19)$$

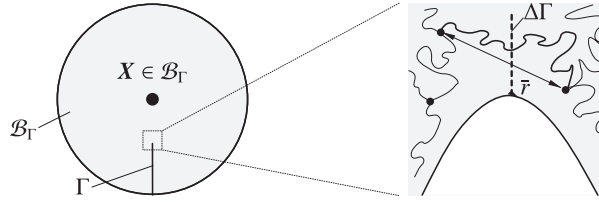


**Fig. 4.** Macro-continuum  $B_\Gamma$  with a crack  $\Gamma$  and zoom out of the deformed crack tip. Chains whose crosslinks lie on opposite sides of a possible extension  $\Delta\Gamma$  of the crack surface  $\Gamma$  must break if crack propagation takes place. This microscopic failure governs the macroscopic critical energy release rate  $g_c$ .

When macroscopic crack propagation occurs on the network scale, a number  $n_\Gamma$  of chains that is crossing a unit area has to be broken to create the new surface  $\Delta\Gamma$ . Assuming a perfectly uniform network such that all chains have the mean end-to-end distance  $\bar{r}$  and contain the same number of monomer units  $N$ , the number of chains crossing unit area is

$$n_\Gamma = \frac{1}{2\bar{r}}n, \quad (20)$$

where  $n$  is again the number of chains per unit volume. With these assumptions, the micromechanically motivated expression for the macroscopic critical energy release rate is for crack propagation in rubbery polymers networks is

$$g_c = n_\Gamma g_{\text{chain}}. \quad (21)$$

Insertion of (20), (19) and (17) into (21) finally gives a micromechanically motivated Griffith-type criterion

$$-\frac{\delta}{\delta\Gamma} E_\Gamma(\varphi) = g_c \quad \text{with} \quad g_c := \sqrt{\frac{2}{3\pi}} \ln N^{3/2} U. \quad (22)$$

The subsequent sections develop a macroscopic phase field model of Griffith-type fracture in rubbers at large strains, which can be linked to the above outlined micro-mechanically approaches of the bulk response and the fracture toughness. In particular, it accounts on the micro-mechanical parameters for the *elastic bulk stiffness*  $\mu$  and the *fracture toughness*  $g_c$  outlined in (9) and (22) above.

### 3. Crack phase field and crack surface density function

#### 3.1. Phase field approximation of crack discontinuities

The idea of regularizing a sharp crack topology by a diffusive crack topology based on the introduction of a *crack phase field*  $d$  was motivated in Miehe et al. (2010b). Let  $\mathcal{B} \subset \mathcal{R}^\delta$  be the reference configuration of a material body with dimension  $\delta \in [2, 3]$  in space and  $\partial\mathcal{B} \subset \mathcal{R}^{\delta-1}$  its surface as depicted in Fig. 5. We consider the time-dependent crack phase field  $d(\mathbf{X}, t)$ , characterizing for  $d=0$  the unbroken and for  $d=1$  the fully broken state of the material at  $\mathbf{X} \in \mathcal{B}$ . In Miehe et al. (2010b), starting from an assumed regularization of a sharp crack at  $x=0$  by the exponential function  $\exp[-|x|/l]$ , a regularized crack surface functional

$$\Gamma_l(d) = \int_{\mathcal{B}} \gamma_l(d, \nabla d) dV \quad (23)$$

was derived in terms of the *crack surface density function* per unit volume of the solid

$$\gamma_l(d, \nabla d) = \frac{1}{2l} d^2 + \frac{l}{2} |\nabla d|^2. \quad (24)$$

This function, which depends on the crack phase field  $d$  and its spatial gradient  $\nabla d$ , plays a critical role in the subsequent modeling of crack propagation. It is governed by the length scale parameter  $l$ . Assuming a given sharp crack surface topology  $\Gamma(t) \subset \mathcal{R}^{\delta-1}$  inside the solid  $\mathcal{B}$  as depicted in Fig. 5, the crack phase field  $d(\mathbf{X}, t)$  on  $\mathcal{B}$  is obtained from the *minimization principle of approximated crack topology*

$$d(\mathbf{X}, t) = \text{Arg} \left\{ \inf_{d \in W_{\Gamma(t)}} \Gamma_l(d) \right\} \quad (25)$$

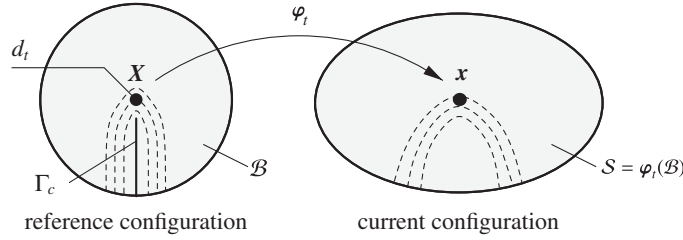


**Fig. 5.** The two basic fields in the phase field modeling of fracture at large strains. The *deformation map*  $\varphi_t$  maps at time  $t \in \mathcal{T}$  the reference configuration  $B \in \mathcal{R}^d$  onto the current configuration  $S = \varphi_t(B)$ . The *crack phase field*  $d_t$  defines a regularized crack surface functional  $\Gamma_l(d)$  which converges in the limit  $l \rightarrow 0$  to the sharp crack surface  $\Gamma$ .

proposed in Miehe et al. (2010b), subject to the Dirichlet constraint  $W_{\Gamma(t)} = \{d | d(\mathbf{X}, t) = 1 \text{ at } \mathbf{X} \in \Gamma(t)\}$ . The Euler equations of this variational principle are

$$d - l^2 \Delta d = 0 \quad \text{in } B \quad \text{and} \quad \nabla d \cdot \mathbf{n} = 0 \quad \text{on } \partial B, \quad (26)$$

where  $\Delta d$  is the Laplacian of the phase field and  $\mathbf{n}$  the outward normal on  $\partial B$ . The above mentioned exponential ansatz is a solution of (26) for the 1D problem with Dirichlet condition  $d=1$  at  $x=0$ . Fig. 6 depicts numerical solutions of the variational problem (25) for 2D problems, which demonstrate the influence of the length scale  $l$ . Note that the limit of the principle (25)

$$\lim_{l \rightarrow 0} \left\{ \inf_{d \in W_{\Gamma(t)}} \Gamma_l(d) \right\} = \Gamma(t) \quad (27)$$

gives for vanishing length scale  $l \rightarrow 0$  the *sharp crack surface*  $\Gamma$  that was used in the micro-mechanical motivation (22), see Fig. 4. A more detailed derivation of the above formulation is outlined in Miehe et al. (2010b).

### 3.2. Crack phase field resistance for brittle fracture

The crack surface density function  $\gamma_l$  defined in (24) provides the starting point for a continuum damage formulation of fracture. In particular, *surface integrals* defined on sharp crack surfaces  $\Gamma \subset B$  are *approximated by volume integrals*, such as the critical fracture surface energy of brittle fracture

$$\int_{\Gamma} g_c dA \approx \int_B g_c \gamma_l dV, \quad (28)$$

where  $g_c$  is the Griffith-type critical energy release with elementary micro-mechanical representation (22). Note that  $g_c \gamma_l$  can be viewed as a *critical fracture energy* measured with respect to the unit volume of the solid's reference configuration. Hence, its evolution can be recast into the form

$$\frac{d}{dt} \int_{\Gamma} g_c dA \approx \int_B g_c \delta_d \gamma_l \cdot \dot{d} dV + \int_{\partial B} g_c (\partial_{\nabla d} \gamma_l \cdot \mathbf{n}) \cdot \dot{d} dA. \quad (29)$$

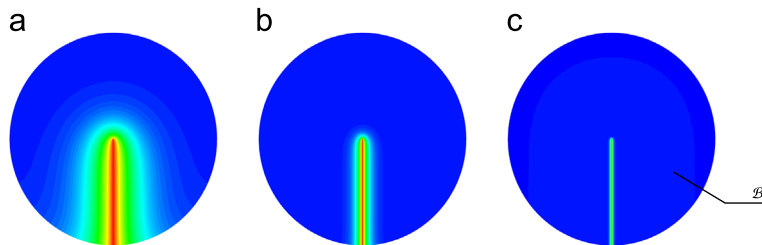


**Fig. 6.** Continuum approximation of crack discontinuities. Solutions of the variational problem (25) of diffusive crack topology for a circular specimen with a given sharp crack  $\Gamma$ , prescribed by the Dirichlet condition  $d=1$ . Crack phase field  $d \in [0, 1]$  for different length scales  $l_a > l_b > l_c$ . The sequence of plots visualizes the limit  $\Gamma_l \rightarrow \Gamma$  of the regularized crack surface functional (23) toward the sharp crack surface.



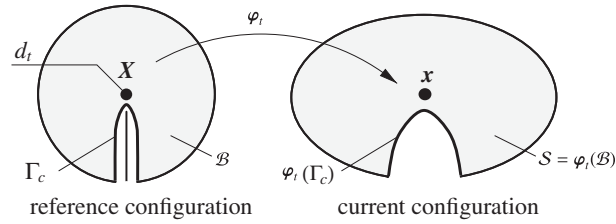


**Fig. 7.** Level set of crack phase field for visualization of crack opening.  $\Gamma_c = \{X | d = c\}$  define the crack faces for  $c = 0.98 \approx 1$ . Parts of the continuum with a crack phase field  $d(\mathbf{X}, t) > c$  above the level set are considered to be free space and are not displayed.

In what follows, we assume *homogeneous Neumann-type boundary conditions* on the surface  $\partial B$  of the reference configuration

$$\partial_{\nabla d} \gamma \cdot \mathbf{n} = l \nabla d \cdot \mathbf{n} = 0 \quad \text{on} \quad \partial B, \quad (30)$$

see Fig. 6. As a consequence, the last term in (29) vanishes and the rate of approximated fracture energy takes the form

$$\frac{d}{dt} \int_{\Gamma} g_c dA \approx \int_B r_l \cdot \dot{d} dV \quad (31)$$

in terms of *crack phase field resistance*  $r_l$ , defined as the dual to the evolution  $\dot{d}$  of the phase field. It is related to the variational derivative of the crack density function  $\gamma_l$  introduced in (24)

$$r_l(d, \Delta d) := g_c \delta_d \gamma_l = \frac{g_c}{l} [d - l^2 \Delta d]. \quad (32)$$

Note that this resistance is a function of the phase field  $d$  and its Laplacian  $\Delta d$ . The definition provides the basis for the construction of a gradient damage theory that is directly rooted in fracture mechanics.

## 4. A framework of diffusive fracture at large strains

### 4.1. The primary fields of the coupled problem

In the large strain context, we describe the response of the fracturing solid by the *deformation field* and the *crack phase field*

$$\varphi : \begin{cases} B \times T \rightarrow \mathcal{R}^d \\ (\mathbf{X}, t) \mapsto \varphi(\mathbf{X}, t) \end{cases} \quad \text{and} \quad d : \begin{cases} B \times T \rightarrow [0, 1] \\ (\mathbf{X}, t) \mapsto d(\mathbf{X}, t). \end{cases} \quad (33)$$

$\varphi$  maps at time  $t \in T$  material points  $\mathbf{X} \in B$  onto spatial points  $\mathbf{x} = \varphi(\mathbf{X}, t)$ .  $d$  determines locally the fractured state of the material point  $\mathbf{X} \in B$  at time  $t \in T$ , that is for  $d=0$  unbroken and for  $d=1$  fully broken. The deformation gradient is

$$\mathbf{F} := \nabla \varphi_t \quad \text{with} \quad J := \det[\mathbf{F}] > 0. \quad (34)$$

The two fields  $\varphi$  and  $d$  are visualized in Fig. 7, where the crack opening is defined by the *level set of the crack phase field*

$$\Gamma_c = \{\mathbf{X} \in B | d(\mathbf{X}, t) = c\}. \quad (35)$$

Here,  $c$  is a constant, for example  $c=0.98$ . Parts of the continuum with a crack phase field  $d(\mathbf{X}, t) > c$  above the level set are considered to be free space and are not displayed. In the current configuration, we recognize the opening of the crack by a separation of the crack faces defined by the level set.

### 4.2. Introduction of energy, dissipation and load functionals

#### 4.2.1. Stored energy functional

We focus on finite elasticity for isotropic solids by considering the global energy storage functional

$$E(\varphi, d) = \int_B \psi(\nabla \varphi, d) dV \quad (36)$$

that depends on the deformation field  $\varphi$  and the fracture phase field  $d$ . The *energy storage function*  $\psi$  describes the energy stored in the bulk of the solid per unit volume. A fully isotropic constitutive assumption for the degradation of energy due to fracture may have the form

$$\psi(\mathbf{F}, d, \nabla d) = [g(d) + k] \psi_0(\mathbf{F}). \quad (37)$$

$\psi_0$  is an isotropic *reference energy function* associated with the undamaged elastic solid, which was micro-mechanically motivated for rubber-like materials in (9), (13) or (14). For the subsequent development, we consider as a model problem the Neo-Hookean function

$$\psi_0(\mathbf{F}) = \frac{\mu}{2} [\text{tr}[\mathbf{F}^T \mathbf{F}] - 3] + \frac{\mu}{\beta} [(\det \mathbf{F})^{-\beta} - 1] \quad (38)$$

with the shear modulus  $\mu > 0$  defined by the Gaussian network model in (9). The parameter  $\beta > 0$  describes a weak volumetric compressibility of the network, and can be linked to the classical Poisson number of linear elasticity via  $\beta = 2\nu/1-2\nu$ . The monotonically decreasing *degradation function*  $g$  describes the degradation of the stored energy with evolving fracture. It is assumed to have the properties

$$g'(d) \leq 0 \quad \text{with} \quad g(0) = 1, \quad g(1) = 0, \quad g'(1) = 0. \quad (39)$$

The first two conditions include the limits for the unbroken and the fully broken case. As shown below, the latter constraint ensures that the energetic fracture force converges to a finite value if the damage converges to the fully broken state  $d=1$ . A simple function that has the above properties is

$$g(d) = (1-d)^2. \quad (40)$$

The small positive parameter  $k \approx 0$  in (37) circumvents the full degradation of the energy by leaving the *artificial elastic rest energy density*  $k\psi_0(\mathbf{F})$  at a fully broken state  $d=1$ . It is chosen as small as possible such that the algebraic conditioning number of the applied numerical discretization method remains well-posed for partly broken systems.

The rate of the stored energy at a given state  $\{\varphi, d\}$  is per definition the time derivative of the energy storage functional (36). We write

$$\mathcal{E}(\dot{\varphi}, \dot{d}; \varphi, d) := \frac{d}{dt} E = \int_B [\mathbf{P} : \nabla \dot{\varphi} - f \dot{d}] dV \quad (41)$$

which is considered to be a functional of the rates  $\{\dot{\varphi}, \dot{d}\}$  at given  $\{\varphi, d\}$ . Here, we introduced per definition the stress tensor

$$\mathbf{P} := \partial_{\mathbf{F}} \psi(\mathbf{F}, d) = [(1-d)^2 + k]\mu[\mathbf{F} - J^{-\beta} \mathbf{F}^{-T}] \quad (42)$$

and the energetic force

$$f := -\partial_d \psi(\mathbf{F}, d, \nabla d) = 2(1-d)\psi_0(\mathbf{F}) \geq 0. \quad (43)$$

As shown in Eq. (58) below, this structure of the energetic force  $f$  with factor  $(1-d)$  ensures the bound of the phase field  $d \rightarrow 1$  for  $\psi_0(\mathbf{F}) \rightarrow \infty$ . The key term that drives the crack evolution is the reference energy  $\psi_0(\mathbf{F})$ , that may be considered to describe locally the intensity of the deformation.

#### 4.2.2. Dissipation functionals

We introduce a *dissipation potential functional* for rate-independent fracture processes at given state  $d$

$$D(\dot{d}; d) = \int_B \phi(\dot{d}; d, \Delta d) dV, \quad (44)$$

which is considered to be a functional to the rate  $\dot{d}$  of the crack phase field, at given  $d$ .  $\phi$  is the *dissipation potential function*. In contrast, the *dissipation functional* is not the time derivative of the dissipation potential functional (44), but defined by the expression

$$\mathcal{D} := \int_B \partial_d \phi \cdot \dot{d} dV. \quad (45)$$

The central demand of the second axiom of thermodynamics is that the dissipation functional has to be positive for all admissible thermodynamic processes

$$\mathcal{D} \geq 0. \quad (46)$$

This inequality serves as a fundamental physically based constraint on the constitutive dissipation potential function  $\phi$ . The thermodynamic condition is a priori satisfied for *normalized, positive* dissipation potential functions which are *convex* with respect to the rate of the constitutive state. The so-called *concept of maximum dissipation* defines the dissipation potential function by the constrained maximum problem

$$\phi(\dot{d}; d, \Delta d) = \sup_{\beta \in \mathbb{E}} \beta \cdot \dot{d} \quad (47)$$

in terms of the variable  $\beta$  dual to  $d$ . It can also be solved by a Lagrange method

$$\phi(\dot{d}, d, \Delta d) = \sup_{\beta, \lambda \geq 0} [\beta \dot{d} - \lambda t_c(\beta; d, \Delta d)] \quad (48)$$

in terms of the driving force  $\beta$  dual to  $d$ , the Lagrange parameter  $\lambda$ , and the *threshold function*  $t_c$  that defines the reversible domain

$$\mathbb{E} := \{\beta | t_c(\beta; d, \Delta d) = \beta - r_l(d, \Delta d) \leq 0\} \quad (49)$$

in the space of the dissipative forces  $\beta$ . Here,  $r_l(d, \Delta d) := g_c \delta_d \gamma_l$  is the *crack phase field resistance function* defined in (32), depending on the macroscopic Griffith-type critical energy release rate  $g_c$  of the polymer network micromechanically motivated in (22). Based on (48), we introduce the *extended dissipation functional*

$$D_\lambda^*(\dot{d}, \beta, \lambda; d) = \int_B [\beta \dot{d} - \lambda t_c(\beta; d, \Delta d)] dV. \quad (50)$$

#### 4.2.3. External load functional

The external mechanical loading is defined by the external load power functional

$$P(\dot{\phi}) = \int_B \bar{\gamma} \cdot \dot{\phi} dV + \int_{\partial B_t} \bar{\mathbf{t}} \cdot \dot{\phi} dA, \quad (51)$$

where  $\bar{\gamma}$  is a given body force field per unit volume and  $\bar{\mathbf{t}}$  a prescribed traction on the surface.

#### 4.3. Rate-type variational principle and governing equations

With the rate of the energy storage functional, the rate of the kinetic energy functional, the extended dissipation functional, and the external power functional at hand, we define the *rate potential functional*

$$\underbrace{\Pi_\lambda(\dot{\phi}, \dot{d}, \beta, \lambda)}_{\text{potential}} = \underbrace{\mathcal{E}(\dot{\phi}, \dot{d})}_{\text{rate of pot. energy}} + \underbrace{D_\lambda^*(\dot{d}, \beta, \lambda)}_{\text{dissipation}} - \underbrace{P(\dot{\phi})}_{\text{external power}} \quad (52)$$

that balances the internal power  $P_{int} = \mathcal{E} + D_\lambda^*$  with the power  $P$  due to external loading. Insertion of the functionals and application of the Gauss theorem gives

$$\begin{aligned} \Pi_\lambda(\dot{\phi}, \dot{d}, \beta, \lambda) = & \int_B \{-[\text{Div}[\partial_{\mathbf{F}}\psi] + \bar{\gamma}] \cdot \dot{\phi}\} dV + \int_B \{[\partial_d \psi + \beta] \dot{d} + (-\beta + g_c \delta_d \gamma_l) \lambda\} dV \\ & + \int_{\partial B_t} [\partial_{\mathbf{F}}\psi \cdot \mathbf{n} - \bar{\mathbf{t}}] \cdot \dot{\phi} dA + \int_{\partial B_f} [\partial_{\nabla d} \psi \cdot \mathbf{n}] \dot{d} dA. \end{aligned} \quad (53)$$

With this potential at hand, we propose the mixed variational principle for the evolution problem

$$\{\dot{\phi}, \dot{d}, \beta, \lambda\} = \text{Arg} \left\{ \underset{\dot{\phi}, \dot{d}, \beta, \lambda \geq 0}{\text{stat}} \Pi_\lambda(\dot{\phi}, \dot{d}, \beta, \lambda) \right\}. \quad (54)$$

The variation of the functional  $\Pi_\lambda$  with respect to the four fields  $\{\dot{\phi}, \dot{d}, \beta, \lambda\}$ , taking into account  $\delta \dot{\phi} = 0$  on  $\partial B_\varphi$ , yields the coupled field equations

$$\begin{aligned} (1): & \quad \text{Div}[\mathbf{P}] + \bar{\gamma} = \mathbf{0}, \\ (2): & \quad \beta - f = 0, \\ (3): & \quad \dot{d} - \lambda = 0, \\ (4): & \quad \lambda \geq 0, \\ (5): & \quad \beta - g_c \delta_d \gamma_l \leq 0, \\ (6): & \quad \lambda(\beta - g_c \delta_d \gamma_l) = 0. \end{aligned} \quad (55)$$

in the domain  $B$  along with the boundary conditions

$$\mathbf{P} \cdot \mathbf{n} = \bar{\mathbf{t}} \quad \text{on } \partial B_t \quad \text{and} \quad \nabla d \cdot \mathbf{n} = 0 \quad \text{on } \partial B. \quad (56)$$

Note that we have introduced per definition the stress tensor  $\mathbf{P}$  and the energetic force  $f$  defined in (42) and (43). The last three equations in (55) are the Kuhn–Tucker-type equations associated with the optimization problem with inequality

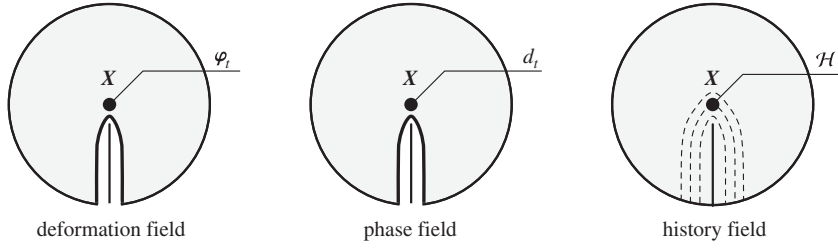


**Fig. 8.** The three fields used for the operator split algorithm in Box 1. The deformation map  $\varphi$ , the fracture phase field  $d$  and the history field  $\mathcal{H}$  are defined at the material point  $\mathbf{X} \in \mathcal{B}$  in the reference configuration  $\mathcal{B}$ . The history field  $\mathcal{H}$  defined in (59) contains a maximum local strain energy obtained within the fracture process.

constraints. From (55)<sub>2,3</sub>, elimination of  $\beta = f$  and  $\lambda = \dot{d}$  yields the reduced system

$$\begin{aligned} (1): & \quad \text{Div}[\mathbf{P}] + \bar{\gamma} = \mathbf{0}, \\ (2): & \quad \dot{d} \geq 0, \\ (3): & \quad f - g_c \delta_d \gamma_l \leq 0, \\ (4): & \quad \dot{d}(f - g_c \delta_d \gamma_l) = 0. \end{aligned} \quad (57)$$

Note that (57)<sub>2</sub> satisfies explicitly the desired thermodynamic consistency condition. The phase field is computed in the case of loading from (57)<sub>4</sub>, which results into

$$r_l := g_c \delta_d \gamma_l := \frac{g_c}{l} [d - l^2 \Delta d] = 2(1-d)\psi_0(\mathbf{F}) \quad \text{for } \dot{d} > 0. \quad (58)$$

Note, that Eq. (58) has the desired property  $d \rightarrow 1$  for  $\psi_0(\mathbf{F}) \rightarrow \infty$ .

#### 4.4. History-field based representation of fracture phase field

We may introduce the *local history field* of maximum positive reference energy of the polymer network

$$\mathcal{H}(\mathbf{X}, t) := \max_{s \in [0, t]} \psi_0(\mathbf{F}(\mathbf{X}, s)) \quad (59)$$

obtained in a typical, possibly cyclical loading process. For a more detailed motivation of the local history field, we refer to the recent work (Miehe et al., 2010a). Replacing  $\psi_0$  in (58) by this field, we obtain the equation

$$\frac{g_c}{l} [d - l^2 \Delta d] = 2(1-d)\mathcal{H}, \quad (60)$$

which determines the phase field in the case of loading *and* unloading. Note that this equation equips the crack topology equation (26)<sub>1</sub> by the local *crack source* on the right hand side. With this notion at hand, the proposed fracture phase field model may be reduced to the compact system of only two equations

$$\begin{aligned} (1): & \quad \text{Div}[\mathbf{P}] + \bar{\gamma} = \mathbf{0}, \\ (2): & \quad g_c \delta_d \gamma_l - 2(1-d)\mathcal{H} = 0, \end{aligned} \quad (61)$$

which determine the current deformation and phase fields  $\varphi$  and  $d$  in terms of the definitions (42), (59) and (58) for the stresses  $\mathbf{P}$ , the history field  $\mathcal{H}$  of maximum reference energy  $\psi_0$  and *crack phase field resistance*  $r_l := g_c \delta_d \gamma_l$  introduced in (32) based on the variational derivative of crack density function  $\gamma_l$  defined in (24). This is considered to be the most simple representation of rate-independent diffusive fracture in rubbery polymers, associated with the multifield scenario visualized in Fig. 8.

#### 4.5. A viscous regularization of the rate-independent problem

An artificial viscous regularization of the above rate-independent formulation of crack propagation in rubbery polymers may stabilize the numerical treatment. To this end, we introduce a *viscous extended dissipation functional* for rate-independent processes

$$D_\eta^*(\dot{d}; \beta; d) = \int_{\mathcal{B}} \left[ \beta \dot{d} - \frac{1}{\eta} \langle t_c(\beta; d, \Delta d) \rangle^2 \right] dV, \quad (62)$$

where  $\langle x \rangle := (x + |x|)/2$  is the ramp function and  $\eta \geq 0$  an artificial viscosity parameter. The corresponding *viscous rate potential functional* reads

$$\underbrace{\Pi_\eta(\dot{\boldsymbol{\varphi}}, \dot{d}, \beta)}_{\text{potential}} = \underbrace{\mathcal{E}(\dot{\boldsymbol{\varphi}}, \dot{d})}_{\text{rate of pot. energy}} + \underbrace{D_\eta^*(\dot{d}, \beta)}_{\text{dissipation}} - \underbrace{P(\dot{\boldsymbol{\varphi}})}_{\text{external power}}. \quad (63)$$

Then the three fields  $\{\dot{\boldsymbol{\varphi}}, \dot{d}, \beta\}$  at a given state are governed by the modified variational principle

$$\{\dot{\boldsymbol{\varphi}}, \dot{d}, \beta\} = \text{Arg} \left\{ \text{stat}_{\dot{\boldsymbol{\varphi}}, \dot{d}, \beta} \Pi_\eta(\dot{\boldsymbol{\varphi}}, \dot{d}, \beta) \right\}. \quad (64)$$

Taking the variation of the potential  $\Pi_\eta$ , we obtain the coupled set of local equations

$$\begin{aligned} (1): \quad & \text{Div}[\mathbf{P}] + \bar{\gamma} = \mathbf{0}, \\ (2): \quad & \dot{d} - \frac{1}{\eta} \langle f - g_c \delta_d \gamma_l \rangle = 0, \end{aligned} \quad (65)$$

where the field  $\beta$  has been eliminated. Note that the evolution  $\dot{d}$  of the phase field is now governed by a viscous equation governed by the ‘over-force’  $\langle f - r_l \rangle$ . As a consequence, (60) may be extended towards a viscous regularized format

$$\frac{g_c}{l} [d - l^2 \Delta d] + \eta \dot{d} = 2(1-d)\mathcal{H}, \quad (66)$$

again driven by the local history field  $\mathcal{H}$  of maximum positive reference energy defined in (59). This equation adds the phase field resistance  $r_l := g_c \delta_d \gamma_l$  defined in (32) the *viscous resistance term*  $\eta \dot{d}$ . Thus the viscous regularization of the system (61) reads

$$\begin{aligned} (1): \quad & \text{Div}[\mathbf{P}] + \bar{\gamma} = \mathbf{0}, \\ (2): \quad & g_c \delta_d \gamma_l + \eta \dot{d} - 2(1-d)\mathcal{H} = 0. \end{aligned} \quad (67)$$

The model is thermodynamically consistent with positive dissipation

$$\mathcal{D} = f \dot{d} \geq 0, \quad (68)$$

which is ensured due to  $f \geq 0$  in (43) and  $\dot{d} \geq 0$  in (65)<sub>2</sub>. Observe that the rate-independent case is recovered by simply setting  $\eta = 0$ . This feature is a very convenient ingredient of a robust numerical implementation.

## 5. Algorithmic formulation of the incremental update problem

We now construct a robust solution procedure of the multifield problem associated with the fields visualized in Fig. 8, based on convenient algorithmic operator splits, in line with the small-strain treatment. The algorithm extends the formulation proposed in Miehe et al. (2010a) from the small-strain setting to finite deformation problems of rubbery polymers. The one-pass split provides two sub-problems for the evolution of the phase field and the deformation field, respectively.

### 5.1. Staggered update scheme of time-discrete fields

#### 5.1.1. Time-discrete fields

We now consider field variables at the discrete times  $0, t_1, t_2, \dots, t_n, t_{n+1}, \dots, T$  of the process interval  $[0, T]$ . In order to advance the solution within a typical time step, we focus on the finite time increment  $[t_n, t_{n+1}]$ , where

$$\tau_{n+1} := t_{n+1} - t_n > 0 \quad (69)$$

denotes the step length. In the subsequent treatment, all field variables at time  $t_n$  are assumed to be *known*. The goal then is to determine the fields at time  $t_{n+1}$  based on variational principles valid for the time increment under consideration. In order to obtain a compact notation, we drop in what follows the subscript  $n+1$  and consider all variables without subscript to be evaluated at time  $t_{n+1}$ . In particular, we write  $\boldsymbol{\varphi}(\mathbf{X}) := \boldsymbol{\varphi}(\mathbf{X}, t_{n+1})$  and  $d(\mathbf{X}) := d(\mathbf{X}, t_{n+1})$  for the deformation and fracture phase field at the current time  $t_{n+1}$  and  $\boldsymbol{\varphi}_n(\mathbf{X}) := \boldsymbol{\varphi}(\mathbf{X}, t_n)$  and  $d_n(\mathbf{X}) := d(\mathbf{X}, t_n)$  for the fields at time  $t_n$ . As a consequence, the rates of the deformation and the fracture phase field are considered to be *constant* in the time increment (69) under consideration, defined by  $\dot{\boldsymbol{\varphi}} := (\boldsymbol{\varphi} - \boldsymbol{\varphi}_n)/\tau$  and  $\dot{d} := (d - d_n)/\tau$ . Note that, due to the given fields at time  $t_n$ , the above rates associated with the time increment (69) are linear functions of the variables at the current time  $t_{n+1}$ .

#### 5.1.2. Update of history field

We consider an operator split algorithm within the typical time step  $[t_n, t_{n+1}]$  that allows a staggered update of the fracture phase field and the deformation field. The central idea for an algorithmic decoupling of the coupled equations is an approximated formulation of the current history field  $\mathcal{H} := \mathcal{H}(\mathbf{X}, t_{n+1})$  in terms of the deformation field  $\boldsymbol{\varphi}_n$  at time  $t_n$  defined in (59). Starting from the initial condition

$$\mathcal{H}_0 := \mathcal{H}(\mathbf{X}, t = t_0) = 0, \quad (70)$$

we assume the current value of maximum reference energy obtained in history to be determined by

$$\mathcal{H} = \begin{cases} \psi_0(\nabla \varphi_n) & \text{for } \psi_0(\nabla \varphi_n) > \mathcal{H}_n, \\ \mathcal{H}_n & \text{otherwise.} \end{cases} \quad (71)$$

As a consequence of this simple definition, the energy  $\mathcal{H}$  that drives the current fracture phase field  $d$  at time  $t_{n+1}$  is in the case of damage loading dependent on the deformation  $\varphi_n$  at time  $t_n$ . With this algorithmic definition at hand, we may define *two decoupled variational problems* which define the phase field  $d$  and the deformation  $\varphi$  at the current time  $t_{n+1}$ .

### 5.1.3. Update of fracture phase field

Considering the energetic history  $\mathcal{H}$  defined in (71) to be *constant* in the time interval  $[t_n, t_{n+1}]$ , we introduce related to (66) the algorithmic functional

$$\Pi_d^\tau(d) = \int_B \left[ g_c \gamma_l(d, \nabla d) + \frac{\eta}{2\tau} (d - d_n)^2 - (1 - d)^2 \mathcal{H} \right] dV, \quad (72)$$

where  $\gamma_l$  is the crack surface density function introduced in (24). The current fracture phase field is then computed from the algorithmic variational problem

$$d = \text{Arg} \left\{ \inf_d \Pi_d^\tau(d) \right\}. \quad (73)$$

The first two terms in the variational functional describe the crack surface resistance and the viscous resistance, respectively. The last term represents the source term governed by the energetic history field  $\mathcal{H}$ . Note that  $\Pi_d^\tau$  is *quadratic*. Hence, the necessary condition of (73) is a simple linear problem for the determination of the current phase field. The Euler equation represents a discretized version of (66). Observe that the rate-independent case is recovered by simply setting the artificial viscous regularization parameter  $\eta = 0$  to zero. This is considered as an important feature of our formulation. No ill-conditioning occurs for the limit  $\eta = 0$ . The viscosity is used as an artificial feature that stabilizes the simulation. It will be chosen as small as possible.

### 5.1.4. Update of deformation field

For a known fracture phase field  $d$  at time  $t_{n+1}$ , we compute the current deformation field  $\varphi$  from the variational principle of finite elasticity. Let

$$\Pi_\varphi^\tau(\varphi) = \int_B [\psi(\nabla \varphi; d) - \bar{\gamma} \cdot \varphi] dV - \int_{\partial B_t} \bar{\mathbf{t}} \cdot \varphi dA \quad (74)$$

be the elastic potential energy at given phase field  $d$ , we get the deformation field from the minimization problem

$$\varphi = \text{Arg} \left\{ \inf_\varphi \Pi_\varphi^\tau(\varphi) \right\} \quad (75)$$

of finite elasticity. Clearly, this problem is non-linear due to the finite strain geometry that underlines the bulk network models of rubber-like polymers outlined in Section 2.

### 5.1.5. Staggered update scheme

The staggered algorithm in the time interval  $[t_n, t_{n+1}]$  is summarized in Box 1. It represents a sequence of two subproblems for the successive update of the fracture phase field and the deformation field. Such an algorithm is extremely robust. Clearly, it may slightly underestimate the speed of the crack evolution when compared with a fully monolithic solution of the coupled problem as considered in Miehe et al. (2010b). However, this can be controlled by making use of adaptive time stepping rules.



## Box 1 Staggered Update Scheme for Phase Field Fracture at Finite Strains.

1. *Initialization.* The deformation, fracture phase and history fields  $\varphi_n$ ,  $d_n$  and  $\mathcal{H}_n$  at time  $t_n$  are known. Update prescribed loads  $\bar{\gamma}$  and  $\bar{\mathbf{F}}$  at current time  $t_{n+1}$ .
2. *Compute History.* Determine maximum reference energy obtained in history
 
$$\mathcal{H} = \begin{cases} \psi_0(\nabla \varphi_n) & \text{for } \psi_0(\nabla \varphi_n) > \mathcal{H}_n, \\ \mathcal{H}_n & \text{otherwise.} \end{cases}$$
 in the domain  $\mathcal{B}$  and store it as a history variable field.
3. *Compute Fracture Phase Field.* Determine the current fracture phase field  $d$  from the *minimization problem of crack topology*

$$d = \text{Arg inf}_d \left\{ \int_{\mathcal{B}} [g_c \gamma_l(d, \nabla d) + \frac{\eta}{2} (d - d_n)^2 - (1 - d)^2 \mathcal{H}] dV \right\}$$
 with critical fracture energy release  $g_c$  and crack surface density function
 
$$\gamma_l(d, \nabla d) = \frac{1}{2l} d^2 + \frac{l}{2} |\nabla d|^2$$
4. *Compute Deformation Field.* Determine the current deformation  $\varphi$  at frozen fracture phase field  $d$  from the *minimization problem of finite elasticity*

$$\varphi = \text{Arg inf}_{\varphi} \left\{ \int_{\mathcal{B}} [\psi(\nabla \varphi; d) - \bar{\gamma} \cdot \varphi] dV - \int_{\partial \mathcal{B}_t} \bar{\mathbf{F}} \cdot \varphi dA \right\}$$
 with the free energy density function
 
$$\psi(\mathbf{F}, d) = [(1 - d)^2 + k] \psi_0(\mathbf{F})$$
 with bulk energy function, e.g.  $\psi_0 = \frac{\mu}{2} [\text{tr}[\mathbf{F}^T \mathbf{F}] - 3] + \frac{\mu}{\beta} [(\det \mathbf{F})^{-\beta} - 1]$ , for the Dirichlet-type boundary condition  $\varphi = \bar{\varphi}$  on  $\partial \mathcal{B}_\varphi$ .

## 5.2. Spatial discretization of the staggered problem

Let  $\mathfrak{T}^h$  denote a finite element triangulation of the solid domain  $\mathcal{B}$ . The index  $h$  indicates a typical mesh size based on  $E^h$  finite element domains  $\mathcal{B}_e^h \in \mathfrak{T}^h$  and  $N^h$  global nodal points. We use the same triangulation for spatial discretization of both the phase field as well as the deformation field.

## 5.2.1. Update of fracture phase field

Associated with  $\mathfrak{T}^h$ , we write the finite element interpolations of the phase field and its gradient by

$$\mathbf{c}_d^h := \{d, \nabla d\}^h = \mathbf{B}_d(\mathbf{X}) \mathbf{d}_d(t) \quad (76)$$

in terms of the nodal phase field vector  $\mathbf{d}_d \in \mathcal{R}^{N^h}$ .  $\mathbf{B}_d$  is a symbolic representation of a global interpolation matrix, containing the shape functions and its derivatives.<sup>1</sup> Introducing the potential density function

$$\pi_d^\varepsilon(d, \nabla d) = g_c \gamma_l(d, \nabla d) + \frac{\eta}{2} (d - d_n)^2 - (1 - d)^2 \mathcal{H}, \quad (77)$$

in (72), the spatial discretization of the variational principle (73) reads

$$\mathbf{d}_d = \text{Arg} \left\{ \inf_{\mathbf{d}_d} \int_{\mathcal{B}^h} \pi_d^\varepsilon(\mathbf{B}_d \mathbf{d}_d) dV \right\}. \quad (78)$$

The associated Euler equation is *linear* and can be solved in closed form

$$\mathbf{d}_d = - \left[ \int_{\mathcal{B}^h} \mathbf{B}_d^T [\partial_{\mathbf{c}_d}^2 \pi_d^\varepsilon] \mathbf{B}_d dV \right]^{-1} \int_{\mathcal{B}^h} \mathbf{B}_d^T [\partial_{\mathbf{c}_d} \pi_d^\varepsilon] dV \quad (79)$$

for the current nodal values of the fracture phase field at time  $t_{n+1}$ .

## 5.2.2. Update of deformation field

Associated with  $\mathfrak{T}^h$ , we write the finite element interpolations of the deformation gradient by

$$\mathbf{c}_\varphi^h := \{\nabla \varphi\}^h = \mathbf{B}_\varphi(\mathbf{X}) \mathbf{d}_\varphi(t) \quad (80)$$

in terms of the nodal position vector  $\mathbf{d}_\varphi \in \mathcal{R}^{\delta N^h}$ . The symbolic global interpolation matrix  $\mathbf{B}_\varphi$  contains the shape functions

<sup>1</sup> Shapes of FE Discretization: For two-dimensional plane strain problems  $\delta = 2$ , the constitutive state vector of the phase field discretization (76) reads  $\mathbf{c}_d = [d, d_{1,1}, d_{2,2}]$ . Then, associated with node  $I$  of a standard finite element  $e$ , the finite element interpolation matrix has the form

$$[\mathbf{B}_d]_I^e = [N \ N_{,1} \ N_{,2}]_I^T$$

in terms of the shape function  $N_I$  at node  $I$  and its derivatives. The state vector of the deformation discretization reads  $\mathbf{c}_\varphi = [\varphi_{1,1}, \varphi_{2,2}, \varphi_{1,2}, \varphi_{2,1}]$  and the associated finite element interpolation matrix has the form

$$[\mathbf{B}_\varphi]_I^e = \begin{bmatrix} N_{,1} & 0 & N_{,2} & 0 \\ 0 & N_{,2} & 0 & N_{,1} \end{bmatrix}_I^T.$$

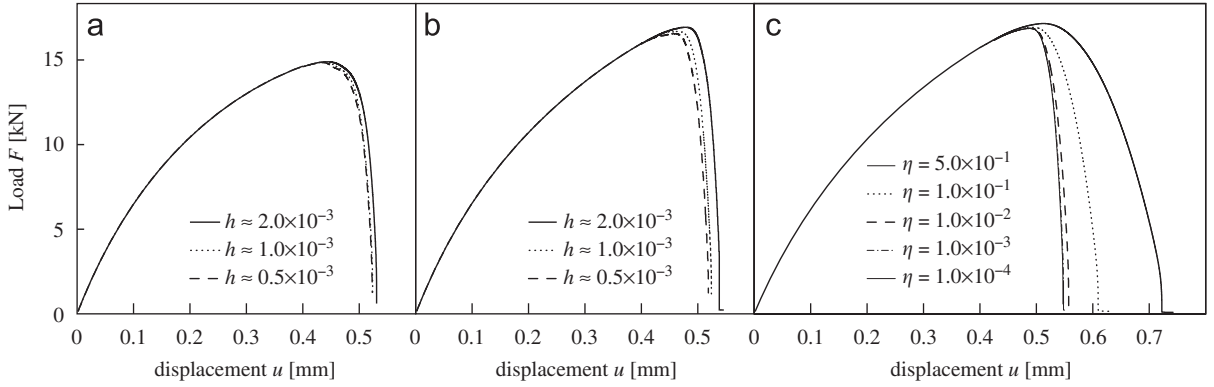


**Fig. 9.** Penny shape tension test. Load deflection curves for simulations with 5000, 15 000 and 45 000 elements carried out with the same viscosity and with the length scales (a)  $l=0.02$  mm and (b)  $l=0.01$  mm. Different artificial viscosities  $\eta$  at length scale  $l=0.01$  mm (c). For vanishing  $\eta$  the graphs converge to the rate-independent limit.

and its derivatives. Introducing the potential density function

$$\pi_\varphi^\tau(\boldsymbol{\varphi}, \nabla \boldsymbol{\varphi}) = \psi(\nabla \boldsymbol{\varphi}; d) - \bar{\gamma} \cdot \boldsymbol{\varphi}, \quad (81)$$

in (74), the spatial discretization of the variational principle (75) reads for a zero traction problem

$$\mathbf{d}_\varphi = \text{Arg} \left\{ \inf_{\mathbf{d}_\varphi} \int_{B^h} \pi_\varphi^\tau(\mathbf{B}_\varphi \mathbf{d}_\varphi) dV \right\}. \quad (82)$$

The associated Euler equation of *non-linear* elasticity at finite strains are solved by a Newton–Raphson iteration based on a sequence of updates

$$\mathbf{d}_\varphi \leftarrow \mathbf{d}_\varphi - \left[ \int_{B^h} \mathbf{B}_\varphi^T [\partial_{\epsilon_\varphi}^2 \pi_\varphi^\tau] \mathbf{B}_\varphi dV \right]^{-1} \int_{B^h} \mathbf{B}_\varphi^T [\partial_{\epsilon_\varphi} \pi_\varphi^\tau] dV \quad (83)$$

for the current nodal values of the deformation field at time  $t_{n+1}$ .

## 6. Representative numerical examples

We now demonstrate the modeling capability of the proposed approach to crack propagation in rubbery polymers at large strains by means of two representative examples. As a first benchmark problem, we consider a penny shape precracked test specimen subjected to tensile loading. Furthermore, we investigate different geometries of a double edge notched specimen in tension that allows to validate the model prediction by comparison with experimental data.

### 6.1. Penny shaped precracked test specimen

We investigate a rectangular plate of 2 mm width and 0.4 mm height with a horizontal notch of 0.2 mm length, placed at middle height in the center of the specimen. The geometric setup is depicted in Fig. 10a. In order to capture the crack pattern properly, the mesh is refined where the crack is expected to propagate. For a discretization with 5000 elements an effective element size of  $h = 2.0 \times 10^{-3}$  mm, for a discretization with 14 000 elements and an effective element size of  $h = 1.0 \times 10^{-3}$  mm and for a discretization with 45 000 elements and an effective element size of  $h = 0.5 \times 10^{-3}$  mm in the critical zone are chosen. The macroscopic shear modulus that had been micromechanically motivated in (9) is chosen to  $\mu = 5$  N/mm<sup>2</sup>. We consider a weakly compressible response with Poisson's ratio  $\nu = 0.45$ . The critical fracture energy, which was micromechanically motivated in (22), is set to  $g_c = 2.4$  N/mm. The computation is performed in a monotonic displacement-driven context with constant displacement increments  $\Delta u = 1 \times 10^{-5}$  mm. In order to point out the effects that arise due to the length-scale parameter  $l$  and the viscosity  $\eta$ , different simulations are performed. The subsequent study analyzes the influence of the discretization on the global response. For the three mesh densities mentioned before, the load deflection curves are compared in Fig. 9a,b for the length scale  $l=0.02$  mm and  $l=0.01$  mm. Obviously, the structural responses show minor difference and the results converge to a solution of finest mesh density. The effect of the regularizing viscosity  $\eta$  on the global response is analyzed in Fig. 9c where the obtained load-deflection curves are depicted for factors  $\eta = 1.0 \times 10^{-4}$ ,  $\eta = 1.0 \times 10^{-3}$ ,  $\eta = 1.0 \times 10^{-2}$ ,  $\eta = 1.0 \times 10^{-1}$  and  $\eta = 5.0 \times 10^{-1}$ . We observe that the curves obtained with the two lowest viscosities almost coincide, and for vanishing viscosity  $\eta \rightarrow 0$  a rate independent limit. For the simulation using an effective element size of  $h = 2.0 \times 10^{-3}$  mm at a length scale of  $l=0.01$  mm the deformed configurations of the specimen at different time steps are depicted in Fig. 10. It shows the crack evolution until the final rupture. The corresponding load-displacement curves are plotted in Fig. 9c. Fig. 10b shows the large deformation of a rubbery polymer. Up to this deformation the fracture phase field is virtually undeveloped. The applied deformation is  $\bar{u} = 0.334$  mm in Fig. 10b. Fig. 10c shows the deformed configuration of the system and the contour of the phase field after an overall deformation of  $\bar{u} = 0.44$  mm.

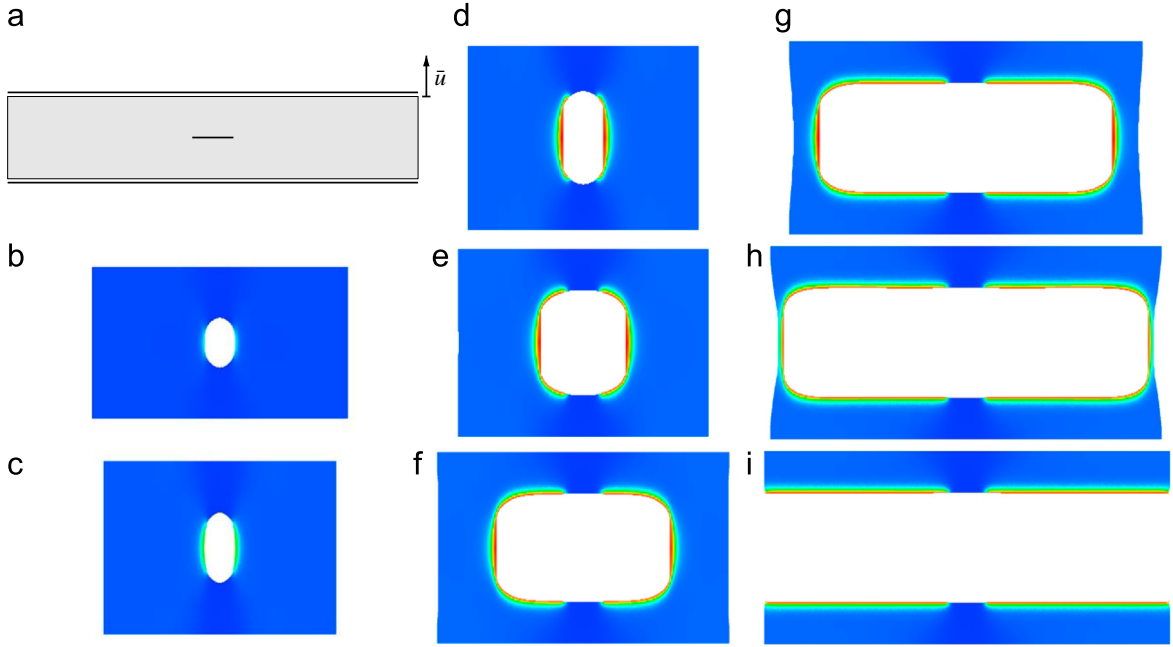


**Fig. 10.** Penny shape tension test. Boundary condition (a). Crack pattern at a displacement of (b)  $\bar{u} = 0.334$  mm, (c)  $\bar{u} = 0.44$  mm, (d)  $\bar{u} = 0.494$  mm, (e)  $\bar{u} = 0.512$  mm, (f)  $\bar{u} = 0.526$  mm, (g)  $\bar{u} = 0.536$  mm, (h)  $\bar{u} = 0.538$  mm and finally (i)  $\bar{u} = 0.5382$  mm for a length scale of  $l = 0.01$  mm and an effective element size  $h = 2 \times 10^{-3}$  mm.

The phase field begins to develop in the area near the initial notch. For an applied deformation of  $\bar{u} = 0.494$  mm the fracture phase field is fully developed in the vicinity of the horizontal notch, Fig. 10d. Once the fracture phase field has reached a value representing fully damaged material, a drastic increase in crack growth occurs. Fig. 10e–i report the system at prescribed boundary displacements of  $\bar{u} = 0.512$  mm,  $\bar{u} = 0.526$  mm,  $\bar{u} = 0.536$  mm,  $\bar{u} = 0.538$  mm and finally  $\bar{u} = 0.5382$  mm. The crack is propagating continuously until the body has separated into two parts.

The technique for the visualization of crack opening, already used in Fig. 10, is explained in Fig. 11 where the contour of the normal stresses and the contour of the fracture-phase-field are depicted. It can be clearly seen that the stresses have the value  $P_{22} = 0$  in the areas where  $d = 1$ . This has to be understood as crack initialization or crack propagation. To visualize the crack opening and the crack growth we exploit the level set function  $\Gamma_c$  introduced in (35). For the visualization of crack opening, the delimitation for continua which have negligible stiffness contribution is chosen at a level set of  $c \geq 0.98$ . Based on this, the contour plots of the fracture phase field are adapted such that the finite elements with a level set of  $c \geq 0.98$  are not displayed. In Fig. 11b this technique is already applied. To make this clear, the real boundary of the continuum is shown with the dashed lines.

## 6.2. Double edge notched specimen in tension

The next benchmark applies the model to five boundary value problems with experimental data available in Hocine et al. (2002). They performed experiments on double edge notch tension specimens to estimate the critical fracture energy. The geometric setup that all the specimen have in common is depicted in Fig. 12a where all dimensions are given in [mm]. The initial crack length  $a$  varies and has the values  $a_i = \{12, 16, 20, 24, 28\}$  mm. In our simulation we exploited the symmetry of the specimen and discretized one quarter of the specimen with approximately 7000–15 000 elements. In order to capture the crack pattern properly, the mesh is refined where the crack is expected to propagate. In the critical zone an effective element size of  $h = 0.05$  mm is chosen. The length-scale parameter applied in the simulations is  $l = 1$  mm resembling 10 elements. The computations are performed in a monotonic displacement driven context with refinement of the displacement increments  $\Delta u$  as soon as the fracture has initiated because of the rapid crack propagation. The elastic constants are  $\mu = 0.203$  N/mm<sup>2</sup> and  $\nu = 0.45$ , the critical fracture energy  $g_c = 2.67$  N/mm. Note, that  $\mu$  and  $g_c$  can be derived from micromechanical quantities of the polymer network according to (9) and (22). The artificial viscosity parameter is chosen to  $\eta = 1.0 \times 10^{-3}$  for all simulation for the five boundary value problems. Fig. 12a shows the load deflection of the experiments and those curves obtained from the simulation for the five specimen geometries. The dotted lines are the load-displacement curves experimentally determined by Hocine et al. (2002), the black curves are the results from the simulations. The geometric setup with the largest initial notch  $a_i = 28$  mm yields the load-displacement curve with the lowest fracture force level. The smaller the initial notch, the higher is the strength of the entire system. When comparing the experimental and the numerical results in Fig. 12b, we observe that the softening effect of the varying initial notch on

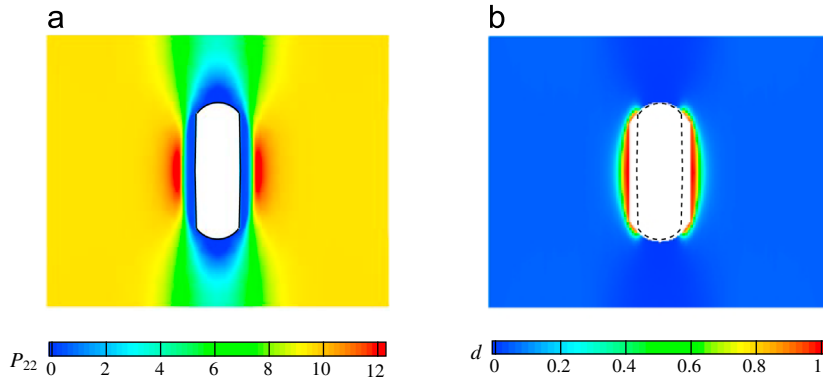


**Fig. 11.** Penny shape tension test. Contour of stresses  $P_{22}$  in direction of the applied deformation at an overall deformation of  $\bar{u} = 0.494$  mm. In the vicinity of the notch the fully developed fracture phase field causes the reduction of material stiffness which is clearly visible through the zero stress value in the vicinity of the initial notch.

the overall system response is captured for all cases in an excellent way. The maximum load that is reached until the rapid crack propagation occurs is predicted by the model in all cases in a very satisfying way. This validates the capabilities of the presented model for the prediction of fracture in rubbery polymers. Finally, Fig. 13 shows the resulting crack pattern with the smallest initial crack  $a = 12$  mm. The visualization of the crack opening and the crack growth exploits the level set function  $\Gamma_c$  introduced in (35). The delimitation of continua which have negligible stiffness contribution is chosen at a level set of  $c \geq 0.98$ . The contour plots of the fracture phase field are adapted such that these areas are not displayed. Fig. 13a–c shows the elastic deformation of the specimen until an overall deformation of  $\bar{u} = 65.44$  mm at which the maximum load is almost reached. The contour plot shows that the phase field is developed to some amount around the initial notch tip. (d) represents the onset of fracture as the phase field exceeds the level set the first time at an overall deformation of  $\bar{u} = 65.608$  mm. After this point the load is drastically decreasing. Fig. 13e–j depict the subsequent propagation of the crack until the body has separated into two parts.

## 7. Conclusion

We outlined a new phase field model for rate-independent crack propagation in rubbery polymers at finite strains and considered details of its numerical implementation. The approach accounts for micro-mechanically based features of both the elastic bulk response as well as the crack toughness of idealized polymer networks. The diffusive crack modeling is governed by a crack phase field that determines a crack density function, which describes the macroscopic crack surface in the polymer per unit of the reference volume. It provides the basis for the constitutive modeling of a degrading free energy storage and a crack threshold function with a Griffith-type critical energy release rate. Both the energy storage as well as the critical energy release due to fracture can be related to classical statistical network theories of polymers. The framework of diffusive fracture

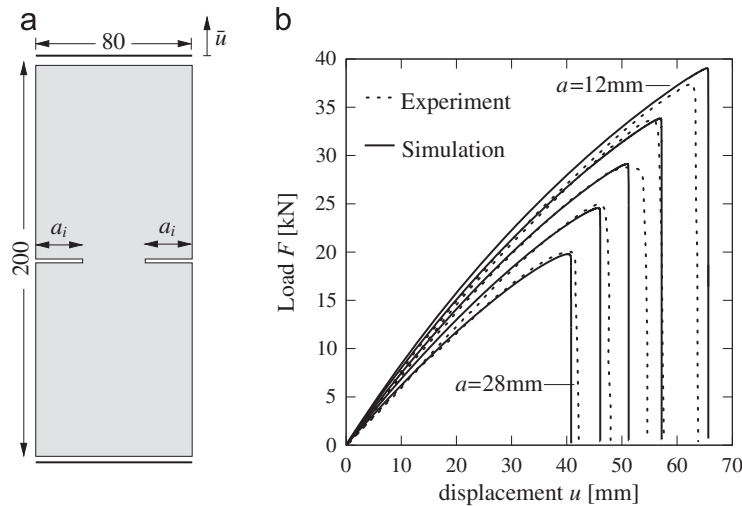


**Fig. 12.** Double edge notch specimen in tension. (a) Boundary conditions and geometry [mm], discretized with quadrilateral elements. Varying initial notch length  $a_i = \{12, 16, 20, 24, 28\}$  [mm], (b) comparison of experimental load–deflection curves from Hocine et al. (2002) with the simulations at chosen material parameter  $l = 1$  mm,  $\mu = 0.203$  N/mm<sup>2</sup>,  $\nu = 0.45$ ,  $g_c = 2.67$  N/mm and  $\eta = 1.0 \times 10^{-3}$ .

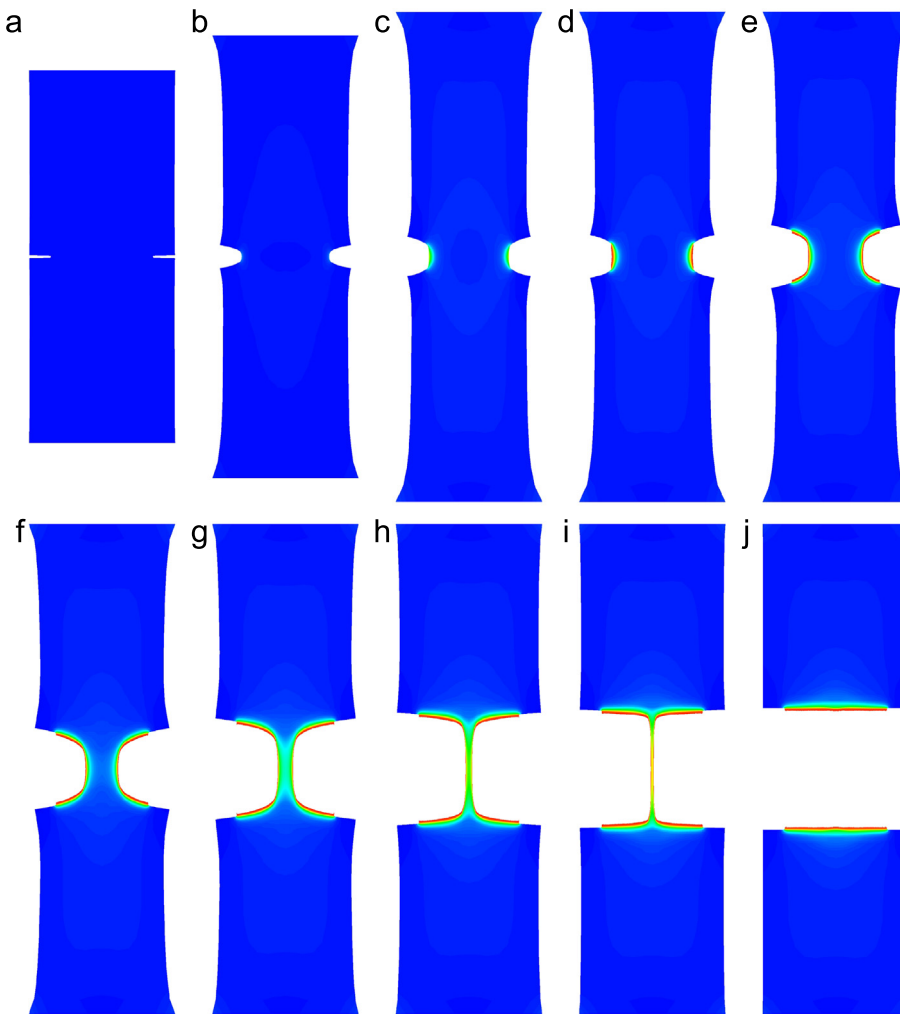


**Fig. 13.** Crack pattern of double edge notch tension specimen with smallest initial notch of 12 mm width. The snapshots (a)–(j) are at applied deformation of  $\bar{u} = 2$ ,  $\bar{u} = 40$ ,  $\bar{u} = 65.44$ ,  $\bar{u} = 65.608$ ,  $\bar{u} = 65.64$ ,  $\bar{u} = 65.646$ ,  $\bar{u} = 65.64816$ ,  $\bar{u} = 65.64848$ ,  $\bar{u} = 65.64852$ ,  $\bar{u} = 65.64854$  [mm]. Effective element size of 0.05 mm and length scale of 1 mm.

in polymers was formulated in terms of a rate-type variational principle that determines the evolution of the coupled primary variable fields. On the computational side, we outlined a staggered solution procedure based on a one-pass operator split of the coupled equations, that successively updates in a typical time step the crack phase field and the displacement field. We finally demonstrated the performance of the diffusive fracture model for rubbery polymers by means of two representative numerical benchmarks. In the second part of this work, we will extend the rate-independent formulation to incorporate dissipative viscous phenomena of the polymer bulk networks, in order to cover a broader spectrum of practical applications.

## Acknowledgments

Support for this research was provided by the German Research Foundation (DFG) under grant Mi 295/13-1.

## References

- Ahagon, A., Gent, A.N., 1975. Threshold fracture energies for elastomers. *J. Polym. Sci. Polym. Phys.* 13, 1903–1911.
- Ambrosio, L., Tortorelli, V.M., 1990. Approximation of functionals depending on jumps by elliptic functionals via  $\gamma$ -convergence. *Commun. Pure Appl. Math.* 43, 999–1036.
- Ambrosio, L., Tortorelli, V.M., 1992. On the approximation of free discontinuity problems. *Boll. UMI* 6-B, 105–123.

- Arruda, E.M., Boyce, M.C., 1993. A three-dimensional constitutive model for the large stretch behavior of rubber elastic materials. *J. Mech. Phys. Solids* 41, 389–412.
- Belytschko, T., Chen, H., Xu, J., Zi, G., 2003. Dynamic crack propagation based on loss of hyperbolicity and a new discontinuous enrichment. *Int. J. Numer. Methods Eng.* 58, 1873–1905.
- Bourdin, B., Francfort, G.A., Marigo, J.-J., 2008. Special invited exposition: the variational approach to fracture. *J. Elasticity* 91, 5–148.
- Boyce, M.C., Arruda, E.M., 2000. Constitutive models of rubber elasticity: a review. *Rubber Chem. Technol.* 73, 504–523.
- Braides, D.P., 1998. *Approximation of Free Discontinuity Problems*. Springer Verlag, Berlin.
- Braides, D.P., 2002.  *$\Gamma$ -Convergence for Beginners*. Oxford University Press, New York.
- Capriz, G., 1989. *Continua with Microstructure*. Springer Verlag.
- Dal Maso, G., 1993. *An Introduction to  $\Gamma$ -Convergence*. Birkhäuser, Boston.
- Deam, R.T., Edwards, S.F., 1976. The theory of rubber elasticity. *Philos. Trans. R. Soc. London A* 280, 317–353.
- Doi, M., Edwards, S.F., 1986. *The Theory of Polymer Dynamics*. Clarendon Press, Oxford.
- Edwards, S.F., Vilgis, T.A., 1988. The tube model theory of rubber elasticity. *Rep. Prog. Phys.* 51, 243–297.
- Flory, P.J., 1989. *Statistical Mechanics of Chain Molecules*. Clarendon Press, Oxford.
- Flory, P.J., Erman, B., 1982. Theory of elasticity of polymer networks. *Macromolecules* 15, 800–806.
- Francfort, G.A., Marigo, J.J., 1998. Revisiting brittle fracture as an energy minimization problem. *J. Mech. Phys. Solids* 46, 1319–1342.
- Frémond, M., 2002. *Non-Smooth Thermomechanics*. Springer Verlag.
- Frémond, M., Nedjar, B., 1996. Damage, gradient of damage and principle of virtual power. *Int. J. Solids Struct.* 33, 1083–1103.
- Gasser, T.C., Holzapfel, G.A., 2005. Modeling 3d crack propagation in unreinforced concrete using PUFEM. *Comput. Methods Appl. Mech. Eng.* 194, 2859–2896.
- Greensmith, H., 1956. Rupture of rubber. iv. tear properties of vulcanizates containing carbon black. *J. Polym. Sci.* 21, 175–187.
- Greensmith, H., Thomas, A., 1955. Rupture of rubber. iii. Determination of tear properties. *J. Polym. Sci.* 18, 189–200.
- Griffith, A.A., 1920. The phenomena of rupture and flow in solids. *Philos. Trans. R. Soc. London A* 221, 163–198.
- Gürses, E., Miehe, C., 2009. A computational framework of three dimensional configurational force driven brittle crack propagation. *Comput. Methods Appl. Mech. Eng.* 198, 1413–1428.
- Hakim, V., Karma, A., 2009. Laws of crack motion and phase-field models of fracture. *J. Mech. Phys. Solids* 57, 342–368.
- Heinrich, G., Kaliske, M., 1997. Theoretical and numerical formulation of a molecular based constitutive tube-model of rubber elasticity. *Comput. Theor. Polym. Sci.* 7, 227–241.
- Heinrich, G., Straube, E., 1983. On the strength and deformation dependence of the tube-like topological constraints of polymer networks, melts and concentrated solutions, i. the polymer network case. *Acta Polymerica* 34, 589–594.
- Hocine, N., Abdelaziz, M., Imad, A., 2002. Fracture problems of rubbers: J-integral estimation based upon  $\hat{I}$ . Factors and an investigation on the strain energy density distribution as a local criterion. *Int. J. Fract.* 117, 1–23.
- James, H.M., Guth, E., 1943. Theory of elastic properties of rubber. *J. Chem. Phys.* 11, 455–481.
- Karma, A., Kessler, D.A., Levine, H., 2001. Phase-field model of mode iii dynamic fracture. *Phys. Rev. Lett.* 87, 045501/1–045501/4.
- Kroon, M., 2011. Steady-state crack growth in rubber-like solids. *Int. J. Fract.* 169, 49–60.
- Kuhn, W., 1934. über die gestalt fadenförmiger moleküle in lösungen. *Kolloid-Zeitschrift* 68, 2–15.
- Kuhn, W., 1936. Beziehungen zwischen molekülgröße, statistischer molekülgestalt und elastischen eigenschaften hochpolymerer stoffe. *Kolloid-Zeitschrift* 76, 258–271.
- Kuhn, W., Gr $\ddot{u}$ n, F., 1942. Beziehungen zwischen elastischen konstanten und dehnungsdoppelbrechung hochelastischer stoffe. *Kolloid-Zeitschrift* 101, 248–271.
- Lake, G., Thomas, A., 1967. The strength of highly elastic material. *Proc. R. Soc. London Ser. A. Math. Phys. Sci.* 300, 108–119.
- Linder, C., Armero, F., 2009. Finite elements with embedded branching. *Finite Elem. Anal. Des.* 45, 280–293.
- Mariano, P.M., 2001. Multifield theories in mechanics of solids. *Adv. Appl. Mech.* 38, 1–93.
- Miehe, C., 2011. A multi-field incremental variational framework for gradient-extended standard dissipative solids. *J. Mech. Phys. Solids* 59, 898–923.
- Miehe, C., Göktepe, S., Lulei, F., 2004. A micro-macro approach to rubber-like materials. part i: the non-affine micro-sphere model of rubber elasticity. *J. Mech. Phys. Solids* 52, 2617–2660.
- Miehe, C., Gürses, E., 2007. A robust algorithm for configurational-force-driven brittle crack propagation with r-adaptive mesh alignment. *Int. J. Numer. Methods Eng.* 72, 127–155.
- Miehe, C., Hofacker, M., Welschinger, F., 2010a. A phase field model for rate-independent crack propagation: robust algorithmic implementation based on operator splits. *Comput. Methods Appl. Mech. Eng.* 199, 2765–2778.
- Miehe, C., Keck, J., 2000. Superimposed finite elastic-viscoelastic-plastoelastic stress response with damage in filled rubbery polymers. experiments, modelling and algorithmic implementation. *J. Mech. Phys. Solids* 48, 323–365.
- Miehe, C., Welschinger, F., Hofacker, M., 2010b. Thermodynamically consistent phase-field models of fracture: variational principles and multi-field FE implementations. *Int. J. Numer. Methods Eng.* 83, 1273–1311.
- Moës, N., Dolbow, J., Belytschko, T., 1999. A finite element method for crack growth without remeshing. *Int. J. Numer. Methods Eng.* 46, 131–150.
- Mueller, H.K., Knauss, W.G., 1971. The fracture energy and some mechanical properties of a polyurethane elastomer. *J. Rheol.* 15, 217–233.
- Ogden, R., 1972. Large deformation isotropic elasticity: on the correlation of theory and experiment for incompressible rubberlike solids. *Proc. R. Soc. London A* 326, 565–584.
- Ogden, R.W., 1984. *Non-linear Elastic Deformations*. Ellis Horwood, Chichester.
- Oliver, J., 1996a. Modelling strong discontinuities in solid mechanics via strain softening constitutive equations. Part 1: fundamentals. *Int. J. Numer. Methods Eng.* 39, 3575–3600.
- Oliver, J., 1996b. Modelling strong discontinuities in solid mechanics via strain softening constitutive equations part 2: numerical simulation. *Int. J. Numer. Methods Eng.* 39, 3601–3623.
- Ortiz, M., Pandolfi, A., 1999. Finite-deformation irreversible cohesive elements for three-dimensional crack-propagation analysis. *Int. J. Numer. Methods Eng.* 44, 1267–1282.
- Peerlings, R.H.J., de Borst, R., Brekelmans, W.A.M., de Vree, J.H.P., 1996. Gradient enhanced damage for quasi-brittle materials. *Int. J. Numer. Methods Eng.* 39, 3391–3403.
- Persson, B.N.J., Albohr, O., Heinrich, G., Ueba, H., 2005. Crack propagation in rubber-like materials. *J. Phys.: Condens. Matter* 17 (44), R1071. URL (<http://stacks.iop.org/0953-8984/17/i=44/a=R01>).
- Persson, B.N.J., Brener, E.A., 2005. Crack propagation in viscoelastic solids. *Phys. Rev. E* 71 (March), 036123. URL (<http://link.aps.org/doi/10.1103/PhysRevE.71.036123>).
- Rivlin, R., Thomas, A., 1953. Rupture of rubber. i. Characteristic energy for tearing. *J. Polym. Sci. X* (3), 291–318.
- Simo, J.C., Oliver, J., Armero, F., 1993. An analysis of strong discontinuities induced by strain-softening in rate-independent inelastic solids. *Comput. Mech.* 12, 277–296.
- Song, J.-H., Belytschko, T., 2009. Cracking node method for dynamic fracture with finite elements. *Int. J. Numer. Methods Eng.* 77, 360–385.
- Thomas, A., 1955. Rupture of rubber. ii. The strain concentration at an incision. *J. Polym. Sci.* 18, 177–188.
- Treloar, L.R.G., 1944. Stress-strain data for vulcanised rubber under various types of deformation. *Trans. Faraday Soc.* 40, 59–70.
- Treloar, L.R.G., 1946. The photoelastic properties of short-chain molecular networks. *Trans. Faraday Soc.* 50, 881–896.
- Treloar, L.R.G., 1975. *The Physics of Rubber Elasticity*, 3rd edition Clarendon Press, Oxford.



- Treloar, L.R.G., Riding, G., 1979. A non-Gaussian theory of rubber in biaxial strain. i. Mechanical properties. *Proc. R. Soc. London A* 369, 261–280.
- Wells, G.N., Sluys, L.J., 2001. A new method for modelling cohesive cracks using finite elements. *Int. J. Numer. Methods Eng.* 50, 2667–2682.
- Wu, P.D., van der Giessen, E., 1993. On improved network models for rubber elasticity and their applications to orientation hardening in glassy polymers. *J. Mech. Phys. Solids* 41, 427–456.
- Xu, X.P., Needleman, A., 1993. Void nucleation by inclusion debonding in a crystal matrix. *Modelling Simul. Materials Sci. Eng.* 1, 111–132.